POLITECNICO DI TORINO
Repository ISTITUZIONALE

Il ruolo culturale delle Piattaforme Digitali per l’esperienza del patrimonio museale | The cultural role of Digital Platforms for the museum heritage experience

Original
Il ruolo culturale delle Piattaforme Digitali per l’esperienza del patrimonio museale | The cultural role of Digital Platforms for the museum heritage experience / Bono, J.. - ELETTRONICO. - (2025), pp. 2335-2358. (46° Convegno Internazionale dei Docenti delle Discipline della Rappresentazione | 46th International Conference of Representation Disciplines Teachers Rome (IT) 11-12-13/09/2025) [10.3280/oa-1430-c877].

Availability:
This version is available at: 11583/3003158 since: 2025-09-19T04:54:22Z

Publisher:
FrancoAngeli

Published
DOI:10.3280/oa-1430-c877

Terms of use:

This article is made available under terms and conditions as specified in the corresponding bibliographic description in the repository

Publisher copyright

(Article begins on next page)

26 November 2026

manuscript fv5124 for review

JOURNAL OF SYNCHROTRON RADIATION

Time and space resolved modelling of the heating induced by synchrotron X-ray nanobeams

Valentina Bonino, Daniele Torsello, Carmelo Prestipino, Lorenzo Mino and Marco Truccato

CONFIDENTIAL – NOT TO BE REPRODUCED, QUOTED NOR SHOWN TO OTHERS

SCIENTIFIC MANUSCRIPT

For review only.

Tuesday 14 July 2020

Category: *research papers*

Co-editor:

Dr V. Favre-Nicolin

ESRF - The European Synchrotron, CS 40220, 38043 Grenoble Cedex 9, France (on leave from Univ. Grenoble Alpes)

Telephone: +33 4 76 88 28 11

Fax: -

Email: favre@esrf.fr

Submitting author:

Valentina Bonino

ESRF - The European Synchrotron, University of Torino, 71 Avenue des Martyrs, Grenoble, Italy, 38000, Italy

Telephone: 0476882095

Fax: +390116707365

Email: valentina.bonino@esrf.fr

This article was prepared with IUCr Journals publication tools

Time and space resolved modelling of the heating induced by synchrotron X-ray nanobeams

Authors

Valentina Bonino[a]*, Daniele Torsello[bc], Carmelo Prestipino[d], Lorenzo Mino[e] and Marco Truccato[fc]

[a]ESRF - The Europan Synchrotron, 71 Avenue des Martyrs, Grenoble, 38000, France

[b]Departement of Applied Science and Technology, Politecnico di Torino, Torino, 10129, Italy

[c] Istituto Nazionale di Fisica Nucleare, Sezione di Torino I, Torino, 10125, Italy

[d]Institut Sciences Chimiques de Rennes, UMR-CNRS 6226, Campus de Beaulieu, Université de Rennes 1, Rennes Cedex, 35042, France

[e]Department of Chemistry and Interdepartmental Centre NIS, University of Torino, via P. Giuria 7, Italy, 10125, Italy

[f]Department of Physics, University of Torino, via P.Giuria 1, Italy, 10125, Italy

Correspondence email: valentina.bonino@esrf.fr

REVIEW DOCUMENT

Synopsis Heating effects of hard X-rays from synchrotron sources are simulated by coupling the Monte Carlo method and the Fourier heat equation. The temperature behaviours simulated are found to be critically dependent on the filling mode of the electron storage ring and on the distribution of the energy density absorbed by the material.

Abstract X–ray synchrotron sources, having high power density, nanometric spot–size and short pulse duration, are extending their application frontiers up to the exploration of direct matter modification. In this field, the use of atomistic and continuum models is now becoming fundamental in the simulation of the photo–induced excitation states and eventually, of the phase transition triggered by intense X-rays. In this work the X-ray heating phenomenon, is studied by coupling the Monte Carlo method (MC) with the Fourier heat equation, to first calculate the distribution of the energy absorbed by the systems and finally predict the heating distribution and evolution. The results of the proposed model are also compared with the ones obtained removing the explicit definition of the energy distribution, as calculated by the MC. A good approximation of experimental thermal measurements produced irradiating a millimetric glass bead is found for both the proposed models. A further step toward more complex systems is done, including in the models the different time-patterns of the source, as determined by the filling modes of the synchrotron storage ring. The two models are applied in three prediction cases, in which the heating produced in $Bi_2Sr_2CaCu_2O_{8+\delta}$ microcrystals by means of nanopatterning experiments with intense hard X–ray nanobeams is calculated. It is demonstrated that the temperature evolution is strictly connected to the filling mode of the storage

IMPORTANT: this document contains embedded data - to preserve data integrity, please ensure where possible that the IUCr Word tools (available from http://journals.iucr.org/services/docxtemplate/) are installed when editing this document.

ring. By coupling the MC with the heat equation, X–ray pulses 48 ps long, having an instantaneous photon flux of about 44 × 10^{13} ph·s^{-1}, were found to be able to induce a maximum temperature increase of 42 K, after a time of 350 ps. Inversely, by ignoring the energy redistribution calculated with MC, peaks temperatures up to hundreds of degrees higher were found. These results highlight the importance of the energy redistribution operated by primary and secondary electrons in the theoretical simulation of the X–ray heating effects.

Keywords: Oxides, radiation damage, Monte Carlo method, finite element method, X-ray nanopatterning

1. Introduction

Since the first–generation synchrotrons, X–ray source characteristics have evolved under the strong demand for higher and higher spatial and temporal resolution. Today, peak brilliances up to 10^{26} photons/s/mm^2/$mrad^2$/0.1% Band Width are achieved with third–generation synchrotron sources, and X–ray beams with nanometric spot–size of about 50–100 nm and pulses of hundreds of ps having energies in the pJ range are routinely achieved (Mino *et al.*, 2018, Martinez-Criado *et al.*, 2016). However, the downside of this ongoing evolution of X–ray sources is that such beam characteristics can exceed the threshold where photon flux density can affect the organization of matter (Bras & Stanley, 2016). As a consequence, the evidences of synchrotron X-ray beams inducing modification phenomena in inorganic materials, such as phase transitions (Adriaens *et al.*, 2013), reduction (Stanley *et al.*, 2014) and crystallization (Feldman *et al.*, 2009, Martis *et al.*, 2011) are now increasing in number. X-ray heating effect is frequently claimed as a possible modification mechanism. So far, however, only few experimental attempts have been made to clarifiy this point. For example, in two thermal imaging experiments (Rosenthal *et al.*, 2014, Snell *et al.*, 2007) carried out on glass beads and on an indium microsized particle, an X-ray heating up to about 30 and 0.2 degrees have been recorded, respectively.

Although more experimental efforts are needed in this direction, nevertheless new research fields are emerging in which X–ray probing and material modification are strictly correlated(Tu *et al.*, 2017, Hsu *et al.*, 2015, Bonino *et al.*, 2019, Pagliero *et al.*, 2014, Truccato *et al.*, 2016, Mino *et al.*, 2017, Mino *et al.*, 2019). In this background, we have recently demonstrated the feasibility of a new patterning concept, based on a resist–free method, which exploits the structural and electrical modifications induced in condensed matter by high–intensity nanometric beams from third–generation synchrotrons (Bonino *et al.*, 2019, Pagliero *et al.*, 2014, Truccato *et al.*, 2016, Mino *et al.*, 2017, Mino *et al.*, 2019). For example, by irradiating the high-temperature superconductors $Bi_2Sr_2CaCu_2O_{8+\delta}$ and $YBa_2Ca_3O_{7-\delta}$ with a 17 keV nanobeam having a flux of about 10^{11} ph s^{-1}, a change of the electrical behaviour was related to an increase of the crystal mosaicity and a depletion of the doping oxygen content (Bonino *et al.*, 2018, Bonino *et al.*, 2019). Following these findings, we

PREVIEW DOCUMENT

exploited these local modifications to nanopattern three $Bi_2Sr_2CaCu_2O_{8+\delta}$ microcrystals, finally fabricating electrical devices based on the Josephson effect (Pagliero *et al.*, 2014, Truccato *et al.*, 2016, Mino *et al.*, 2017).

Despite all the experimental evidences of photoinduced phenomena, due to the large variety of X–ray–matter interaction mechanisms that can be accessed with high–intensity X-rays, a clear picture of the mechanisms involved in material modification is still missing. Depending on the beam intensity and pulse duration, both reversible and irreversible matter states can be induced in a variety of inorganic materials (London *et al.*, 2001, Hau-Riege, 2012). This is not surprising, indeed similar concepts have been extensively investigated in the field of high–power laser irradiaton, where both thermal and non–thermal effects are currently exploited in many laser–based technological processes (Mirzoev *et al.*, 1996, Liu *et al.*, 1997).

The similarities between high–intensity synchrotron X–ray and optical and IR laser irradiations are several. As in femtosecond lasers, X–rays ionize the matter, but differently from them, they excite the inner–shells of the atoms and penetrate in–depth in the material volume. In the femtosecond scale, the absorbed X–ray energy is dissipated through the emission of fluorescent photons and of Auger and photo–electrons. Then a cascade of excitation processes is initiated by electrons and eventually, in the picosecond timescale, they thermalize firstly among themselves and then with the lattice. Another difference with lasers concerns the surface power densities that can be delivered with a single pulse. Femtosecond lasers can reach 10^{22} W/cm^2 (Bahk *et al.*, 2004), while the picosecond pulses of third-generation synchrotron can only achieve values in the order of 10^{14} W/cm^2. For all of these reasons, although many concepts valid for high–power lasers can be extended to the X–ray regime, differences in thermal distribution are expected and a simple extrapolation from laser data will not work. In this sense, more efforts are necessary from the theoretical point of view to fully understand the effects of high–intensity X–ray/matter interactions.

Both space and time scales are important in determining the simulation method to approach numerically the problem. Molecular dynamics and Monte Carlo methods (MC), simulating respectively the motion of atoms, ion and molecules, and the transport of photons and electrons, are applied in systems with sizes up to the micrometric range for fast processes with a maximum time limit in the picosecond scale (Gnodtke *et al.*, 2009, Neutze *et al.*, 2000, London *et al.*, 2001). As an example, by considering the Seitz-Koehler cross-section(Seitz & Turnbull, 1956), that accounts for the atom knock–on by photoelectrons, in a previous study we applied the Monte Carlo method to simulate the displacement of the oxygen–doping content to non–active doping positions in $Bi_2Sr_2CaCu_2O_{8+\delta}$ microcrystals. This mechanism was found to be the principal responsible for the photo–induced resistivity change for a fraction of the investigated experimental cases (Torsello *et al.*, 2018). For larger scales, once the electrons have thermalized, continuum models are preferred to simulate effects such as melting and cracking (Nicholson *et al.*, 2001, Mino *et al.*, 2017, Wallander &

REVIEW DOCUMENT

Wallentin, 2017, London *et al.*, 2001). As an example, by means of finite element method we solved the heat equation for an X–ray nanopatterning experiment, calculating the temperature modulation generated by synchrotron pulses (Mino *et al.*, 2017). Similarly, Wallander and Wallentin in their work (Wallander & Wallentin, 2017) modelled the temperature increase induced in an InP nanowire. However, in these cases the derived heating was calculated implementing a heat source implicitly defined as the product between the beam profile and the decaying profile of X-rays as defined by the attenuation length coefficient, i.e. without taking into account the details of the fraction of absorbed photons and of the spatial distribution of the absorbed energy—.

In the present work, by continuing our efforts toward the simulation of the heating effects induced by intense X-rays, we want to assess the temperature increase in both space and time in more details. For the purpose, by considering for the first time both the spatial distribution of the absorbed energy and the real time–structure of synchrotron radiation, a more accurate numerical model has been formulated in which the heat source is modulated in both space and time. This was achieved by coupling the radiation–particle transport problem, solved with the Monte Carlo method, with the time–dependent heat equation. With such a detailed model, the temperature increase can be calculated with an unprecedented accuracy. For comparison, the heat equation is also solved implicitly defining the heat source with the aforementioned method, already adopted in literature.

In the following, the model validation and accuracy are first discussed by modelling the first thermal imaging experiment reported in 2006 by Snell et al. (Snell *et al.*, 2007). The temperature transient, experimentally monitored by the authors, is compared with the one predicted by the model. Then, three examples of X-ray nanopattering on $Bi_2Sr_2CaCu_2O_{8+\delta}$ microcrystals (Pagliero *et al.*, 2014, Truccato *et al.*, 2016, Mino *et al.*, 2017) are considered to discuss the role of heating on the structural and electrical modifications observed in the fabrication process. For the purpose, the stationary, the transient and pulsed regimes of the thermal model are separately treated.

2. Method

2.1. Experimental methods for validation and prediction

Based on their scope, the cases considered can be divided into two categories: validation and prediction. In the validation case, the irradiation of a glass bead (composition in mass percentage: 66% SiO_2,15% Na_2O, 7% CaO, 5% Al_2O_3, 3% B_2O_3, 2% ZnO, 1% K_2O,and 1% MgO) (Snell *et al.*, 2007), at ambient temperature is implemented. In Table 1 the main experimental parameters are summarized. The modelling method used for this case is based on the definition of a range of validity in which the solutions can lie. The range is defined by varying the experimental parameters within their experimental error (reported in table 1). The complete experimental method can be found in the reference work (Snell *et al.*, 2007). Conversely, the three X-ray nanopatterning experiments fall within the prediction category. In these cases, no experimental measurements of the temperature are

REVIEW DOCUMENT

given. Therefore, the related simulations have the unique purpose of estimating the temperatures reached during the patterning process. These experiments were directly performed by the authors at the European Synchrotron Radiation Facility (ESRF, Grenoble, France). The experimental details are reported in the following.

To ensure continuity with the previous works, the $Bi_2Sr_2CaCu_2O_{8+\delta}$ samples are named following the same sample nomenclature: WBVB08 (Mino *et al.*, 2017), WBAP13 (Pagliero *et al.*, 2014), and WBAP14 (Truccato *et al.*, 2016). Respectively: (i) WBVB08 was irradiated at the beamline ID16B using a pink beam ($\Delta E/E \approx 10^{-2}$) and a 16-bunch filling mode of the storage ring having a maximum current of 90 mA. This filling mode consists of a train of sixteen equally spaced, highly populated electron bunches, each of them generating a current equal to 90 mA/16 bunch =5.625 mA/bunch and a Gaussian time profile for the corresponding X–ray pulse with a rms duration $RMS_t \approx 48$ ps. (ii) WBAP13 was irradiated at the ID22 beamline with a monochromatic beam ($\Delta E/E \approx 10^{-4}$) with 16-bunch filling mode. (iii) WBAP14 was irradiated at the beamline ID16B using a pink beam ($\Delta E/E \approx 10^{-2}$) with a 7/8+1 filling mode of the storage ring. This mode consists in filling 7/8 of the storage ring length with 868 equally spaced bunches of 0.23 mA/bunch, having at their extremes two bunches of 1 mA. The remaining 1/8 of the storage ring is filled in its centre by a single bunch of 2 mA. This results in a typical rms duration of the pulses $RMS_t \approx 20$ ps. The samples dimensions are reported in Table 1 together with the experimental beam parameters: time-averaged photon flux $\bar{\Phi}_0$, photon energy E_0 and beam size.

Table 1 Experimental parameters used for the validation and the prediction cases. w and t are the width and the thickness of the samples, while for the bead w refers to the diameter. $\bar{\Phi}_0$ represents the time-averaged photon flux and E_0 is the photon energy. V × H are the horizontal and vertical values of the FWHM of the Gaussian beam profile, as measured by the knife edge method. V and H were aligned with the *x*– and *z*–axes of the geometrical model.

Sample	w (μm)	t(μm)	$\bar{\Phi}_0$ (ph/s)	E_0 (keV)	V (μm)× H(μm)	Filling mode	Ref
Bead	2000 ±10%		3.24×10^{12} ±15%	*6.5*	84 × 103	-	(Snell *et al.*, 2007)
WBVB08	6.71	0.38	3.0×10^{11}	17.4	0.050 × 0.070	16-bunch	(Mino *et al.*, 2017)
WBAP13	13.55	1.6	1.9×10^{11}	17.05	0.117 × 0.116	16-bunch	(Pagliero *et al.*,

REVIEW DOCUMENT

							2014)
WBAP14	4.88	1.6	1.0×10^{11}	17.6	0.057 × 0.045	7/8+1	(Truccato *et al.*, 2016)

An overview of a typical $Bi_2Sr_2CaCu_2O_{8+\delta}$ chip is reported in Figure 1(a). The irradiated region is located between the voltage electrodes (framed in black) and X–rays impinged on the *ac*–crystallographic plane. As determined during SEM analysis, this region consists of a section of the $Bi_2Sr_2CaCu_2O_{8+\delta}$ crystal mounted on top of a sapphire substrate (0.5 mm thick) and separated from it by a thin layer of air about 1 μm in thickness.

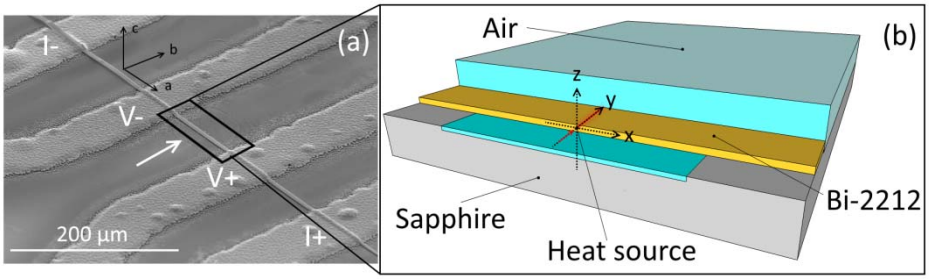


Figure 1 (a) Scanning Electron Microscope (SEM) micrograph of a typical measurement chip (WBVB08). The current and voltage Ag electrodes are labelled as I+, I- and V+, V-, respectively. The arrow represents the synchrotron nanobeam used for crystal irradiation. (b) 3D model used for FEM simulations. Sapphire pads under the $Bi_2Sr_2CaCu_2O_{8+\delta}$ crystal represent the regions of strong thermal contact between substrate and crystal. As observed at the SEM, a 1-μm thick air layer is present under the crystal between these two pads to take into account the poor thermal contact between crystal and substrate. The air layer above the crystal is 100–μm thick (not to scale) and the sapphire substrate is 100–μm thick (not to scale). The red solid arrow indicates the position and direction of the nanobeam. *x*–, *y*–, and *z*–axes of the reference frame are oriented along the *a*–, *b*–, and *c*–crystallographic axes, respectively.

2.2. Simulation strategy and geometry

The selection of the simulation method is based on the analysis of the de–excitation processes. The electron relaxation time τ_{el} during which non–thermal phenomena can be observed is less than 1 ps for the systems considered (Lindgren *et al.*, 1999, Truccato *et al.*, 2006, Medvedev, 2015 #302, Kaiser, 2000 #360), while the timescale of the heating process is defined by the electron–lattice thermalization $\tau_{el\text{-}ph}$, which is typically few ps long (Lindgren *et al.*, 1999, Truccato *et al.*, 2006, Gadermaier *et al.*, 2010 Medvedev, 2015 #302, Kaiser, 2000 #360). These timescales must be

compared with the duration of the X–ray pulse length $t_p \approx 2.35 \times RMS_t$. Synchrotrons have t_p values in the order of tens of ps, therefore, in the first instants of the pulse the sample rapidly reaches the electron–lattice equilibrium and then starts dissipating the absorbed energy by following the thermal route. Accordingly, the spatial dispersion of the absorbed energy within the target, triggered by the emission of photo– and Auger electrons, starts well before the thermal de–excitation process. We have already explored the concept of energy dispersion by means of radiation–transport simulations of the X-ray nanopatterning process, founding that the photogenerated electrons exist well beyond the exposed volume, and can spread around up to 200 nm from the beam centre (Torsello *et al.*, 2018). Based on these considerations, the fraction of absorbed energy and its spatial distribution, due to the quick electron relaxation mechanisms, must be considered to calculate in an accurate way the slower and consequent temperature increase. Therefore, the new simulation strategy proposed relies on the coupling of the radiation– and heat–transport physics.

In the present work, when the distribution of the absorbed X–ray energy is considered, it was calculated through Monte Carlo method using the MCNP6 code (T. Goorley *et al.*,). Each geometry was confined to the region interested by the radiation and particles transport. Each physical event was tracked by means of a mesh of elementary cubic volumes, called voxels. In order to reach a good compromise between space resolution and computation time, the size of voxels edges was fixed to 50 nm.

The heat–transport was calculated with the finite element method with the software COMSOL Multiphysics (*COMSOL Multiphysics*®). The heating source was implemented in agreement with the distribution of energy calculated by means of the radiation–transport simulation. The origin of the frame of reference was set to coincide with the point where the beam strikes the samples. Concerning the geometries, to model the heating of the glass bead two concentric spheres were used. The inner one represents the glass domain of the bead, and the outer one the surrounding air domain. The volume of the air domain was fixed to be 20 times the bead radius to safely exclude any influence of the boundary conditions on the results. For the prediction cases, the geometry implemented is more complex and reports only the regions of interest (see Figure 1(b)). It consists of a 140 μm-long $Bi_2Sr_2CaCu_2O_{8+\delta}$ crystal, representing the crystal portion between the voltage electrodes, surrounded by air (100 μm thick) and by the sapphire substrate (100 μm thick). The silver electrodes were not reported in the models because their distance from the irradiated region (≈ 70 μm) is large enough not to affect the quality of the results. The thermal contact between crystal and substrate, which is guaranteed in the proximity of the silver electrodes, was represented by means of two sapphire pads located at the extremities of the crystal length (see Figure 1(b)).

2.2.1. MCNP6 code

REVIEW DOCUMENT

In MCNP6 code, both the photo–atomic interactions (photoelectric effect, Compton scattering, coherent and incoherent scattering) and the electron interactions (electron energy loss, electron angular deflection, Bremsstrahlung emission, Auger electron, knock-on of electrons) are considered. However, some approximations are made. The crystal structure of the material is not taken into account, so that the materials are always considered as amorphous. Moreover, a low–energy threshold of 1 keV is applied for particle tracking, which neglects the fact that the low–energy particles can move further in space and therefore slightly over–confines energy deposition by the beam in the material.

The photon source was defined specifying the energy of the impinging photon E_0, and the experimental Gaussian profile of the X–ray beam (see Table 1). The latter was approximated by a 2D Gaussian function as follows:

$$I(x,z) = \frac{2}{\pi W_x W_z} e^{-\left(\frac{2x^2}{W_x^2}+\frac{2z^2}{W_z^2}\right)} \quad (1)$$

with W_x and W_z defined as $W_i = \frac{FWHM_i}{\sqrt{2ln2}} \cong 0.85 \cdot FWHM_i$, and $FWHM_i$ corresponding to the beam sizes of Table 1.

The deposited energy density for each voxel is expressed per impinging photon $E(x,y,z)$. In order to reach a valid statistical result, the final spatial distribution was calculated with a total number of 10^8 trial photons.

Concerning the photoexcitation conditions, an important difference exists between the validation and the prediction cases. In the former, the ratio between the radial redistribution of the deposited energy, being of few hundreds of nanometres wide (see Figure S1, in the supporting information), and the micrometric beam size, is very small. Therefore, for this case the contribution of photo– and secondary electrons is expected to play a minor role in the heating effects. Secondly, because both the beam size and the attenuation length are much smaller than the sample diameter, an important fraction of the volume is not interested by the relaxation phenomena considered in the MCNP6 code. On the contrary, in the latter cases, along the direction perpendicular to the beam, the spatial length of the energy redistribution processes is comparable with the nanometric dimension of the spot size. This is represented in Figure 2, in which the energy density distribution for the prediction cases WBVB08, WBAP13 and WBAP14 is reported as a function of the beam penetration direction *y* and of the two perpendicular directions *z* (panels (a), (b), (c)) and *x* (panels (d), (e), (f)), respectively. The effects of energy dissipation are evident in the distribution widths, which are wider than the corresponding FWHM of the beam profile. Nonetheless, the energy density distributions are still correlated with the beam shape. This is highlighted by the fact that the lateral spread of the energy densities rescales coherently with the X–ray beamsize adopted in each experiment. Finally, on the beam direction, a

REVIEW DOCUMENT

fraction of the incident energy is transmitted. Form these calculations, it is visible how in these cases an accurate definition of the energy distribution becomes important.

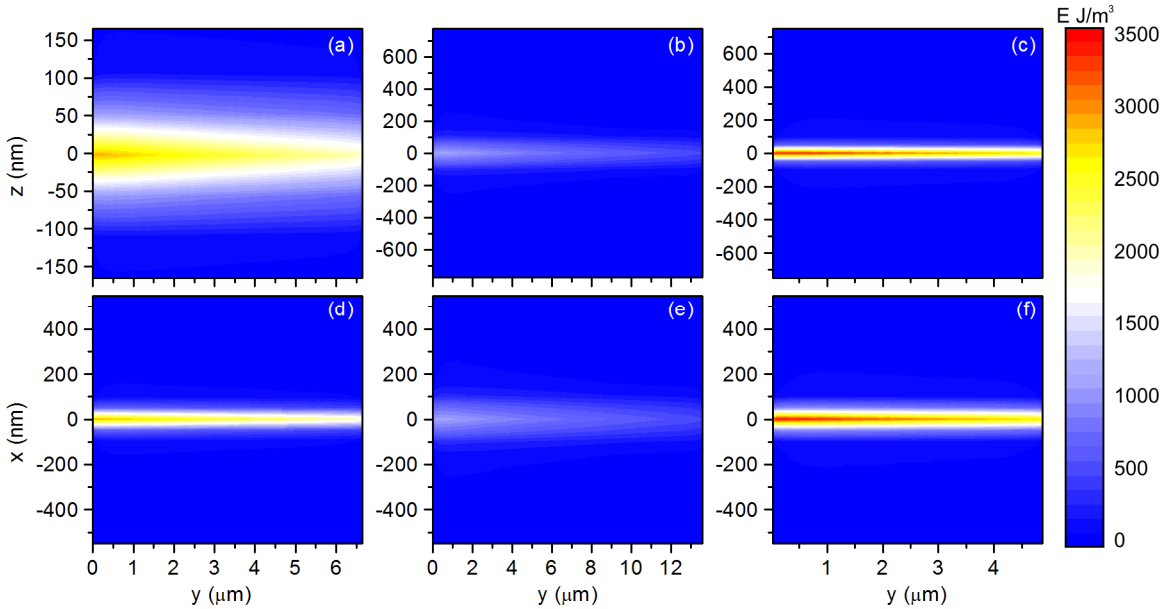


Figure 2 2D plots of the energy spatial distributions evaluated by the MCNP6 code. Respectively for samples WBVB08, WBAP13, and WABAP14: panels (a), (b), (c) show the *zy* cross-sections (x=0) of the model, corresponding to the *bc*–plane of the crystals (the z–direction is aligned with sample thickness), and panels (d), (e), (f) show the *xy* cross-sections (z=0), corresponding to the *ab*-plane of the crystals.

In Table 2 the peak values of the energy density distributions (E_{max}) are summarized for each sample.

Table 2 Maximum energy values E_{max} derived from the MC simulations reported in Figure 2, and the corresponding maximum power density values $\bar{P}_{ex\ max} = \bar{\Phi}_0 E_{max}$. The maximum of the power density for the implicit case $\bar{P}_{im\ max}$ is also reported. Additionally, also the E_{max} value of the validation case of Figure S1 is shown.

Sample	E_{max} (J/m^3)	$\bar{P}_{ex\ max}$ (W/m^3)	$\bar{P}_{im\ max}$ (W/m^3)
Bead	1.470×10^{-3}	4.8×10^{9}	6.7×10^{9}
WBVB08	2920	8.8×10^{14}	1.2×10^{16}
WBAP13	1140	2.2×10^{14}	1.9×10^{15}
WBAP14	3500	3.5×10^{14}	5.6×10^{15}

2.2.2. COMSOL model

Since t_p is much greater than both τ_e and $\tau_{el\text{-}ph}$, the classical Fourier heat diffusion equation should provide a good description of the temperature evolution. The Fourier heat equation is then used:

$$\rho C_p \frac{\partial T}{\partial t} + \nabla \cdot (-k \nabla T) = Q \quad (2)$$

where T represents the space and time-dependent temperature field, ρ, C_p and k are respectively the density, the heat capacity at constant pressure, and the thermal conductivity of the materials (see values listed in Table 3) , and Q represents the heat source. The thermal coefficients of the materials were supposed to be constant in the temperature range of interest. Boundary conditions were assumed by imposing a constant temperature, equal to the ambient temperature, on all the model external boundaries.

Table 3 Thermodynamic properties of materials at ambient temperature used in the model

Material	ρ (kg m^{-3})	C_p (J kg^{-1} K^{-1})	k (W m^{-1} K^{-1})
Glass bead	2500 (Snell *et al.*, 2007)	799 (Snell *et al.*, 2007)	0.97 (Snell *et al.*, 2007)
$Bi_2Sr_2CaCu_2O_{8+\delta}$	6700 (Subramanian *et al.*, 1988)	450 (Natividad *et al.*, 2006)	0.88 (c-plane), 6.29 (ab-axis) (Crommie & Zettl, 1990)
Sapphire	4000 (Burghartz & Schulz, 1994)	780 (Archer, 1993)	40 (Burghartz & Schulz, 1994)
Air	1.2 (US Standard Atmosphere, 1976)	1012 (Lide, 2003)	0.026 (Lide, 2003)

In the explicit case, the heat source Q of the FEM model was set equal to the power density absorbed by the crystal $P_{abs\ ex}$:

$$Q_{ex}(x,y,z,t) = P_{abs\ ex}\ (x,y,z,t) = \Phi(t)E(x,y,z) \quad (3)$$

with $\Phi(t)$ the instantaneous photon flux and $E(x,y,z)$ the deposited energy density distribution as calculated by MC simulations. Moreover, in order to highlight the impact of the MC simulation in the X-ray heating process, the same model was also solved ignoring the physics of the beam–crystal interaction. In this case, the space distribution of the heating power Q was implicitly considered equal to the space distribution of the X-ray absorption, as emerging from the experimental conditions. Therefore, along the beam direction (i.e. the y-axis) the power absorbed was represented in agreement with the Lambert-Beer law, and along the two directions normal to the beam direction, it was defined by means of the experimental intensity profile of the incident beam (Equation (1)). The final form of the implicit definition of the heat source is equal to:

REVIEW DOCUMENT

$$Q_{im}(x,y,z,t) = P_{abs\,im}(x,y,z,t) = \frac{2\Phi(t)E_0}{\pi W_x W_z \lambda} e^{-\left(\frac{y}{\lambda}+\frac{2x^2}{W_x^2}+\frac{2z^2}{W_z^2}\right)} \quad (4)$$

Where parameter λ represents the attenuation length of the material (51 μm for glass and around 17 μm for $Bi_2Sr_2CaCu_2O_{8+\delta}$ (Henke, 1993)). For simplicity, in the following we will refer to the two approaches, resulting from the use of the two heat sources Q_{ex} and Q_{im} , as the explicit and implicit methods, respectively.

By substituting the instantaneous photon flux $\Phi(t)$ with the experimental time-averaged photon flux $\bar{\Phi}_0$ (see Table 1), the total time–averaged power density absorbed by the samples was obtained. In Table 2, with $\bar{P}_{im\ max}$ and $\bar{P}_{ex\ max}$ the corresponding maximum values are reported for the implicit and the explicit methods, respectively.

Few hundreds of thousands of elements were created in the mesh, and a computer having 88 Gb of RAM and two processors with a clock of 2.4 GHz was used for the calculations. The computing time for all the simulations did not exceed 12 hours.

3. Result and discussion

3.1. Validation case

We have carried out the simulation corresponding to the validation case by calculating the transient behaviour induced in the experimental conditions of Ref. (Snell *et al.*, 2007) in the presence of a time-averaged photon flux $\bar{\Phi}_0 = 3.24\times10^{12}$ ph/s (see Table 1). In Figure 3, the evolution of the experimental (dots) and the calculated (lines) heating for the glass bead is reported within the first 5 s of irradiation. The data refer to the average temperature at the sample surface in the area impinged by the beam. The solid lines define the limits of the range (highlighted in grey) of all of the possible behaviours predicted with the explicit method. The upper and the lower limits were found by considering the experimental ranges shown in Table 1. A good agreement between experimental and calculated behaviours is observed. Indeed, except for the first instants of irradiation, the experimental data fall inside the simulated range. It is also important to note that, if other experimental uncertainties were implemented, the range of existence of the simulated behaviour (which was found considering only the variations in the sphere diameter and in the photon flux) would be even wider. Among the uncertainties, the geometry and materials of the sphere holder, the shape irregularities present in the sample geometry, and the imperfect alignment of the beam direction with the centre of the bead, would certainly play a role in increasing further the grey area of Figure 3. This means that to have an accurate prediction of the X-ray heating, all the experimental parameter must be carefully controlled and the experimental uncertainties minimized.

In Figure 2, the theoretical behaviour predicted by the implicit method is also reported with the dashed lines. As expected, the heating for the implicit method is greater than the one calculated with

REVIEW DOCUMENT

the explicit method. However, this is coherent with the fact that the ratio between the nanometric length of the diffusive behaviour of the relaxation phenomena and the micrometric dimension of the X–ray beam is very small.

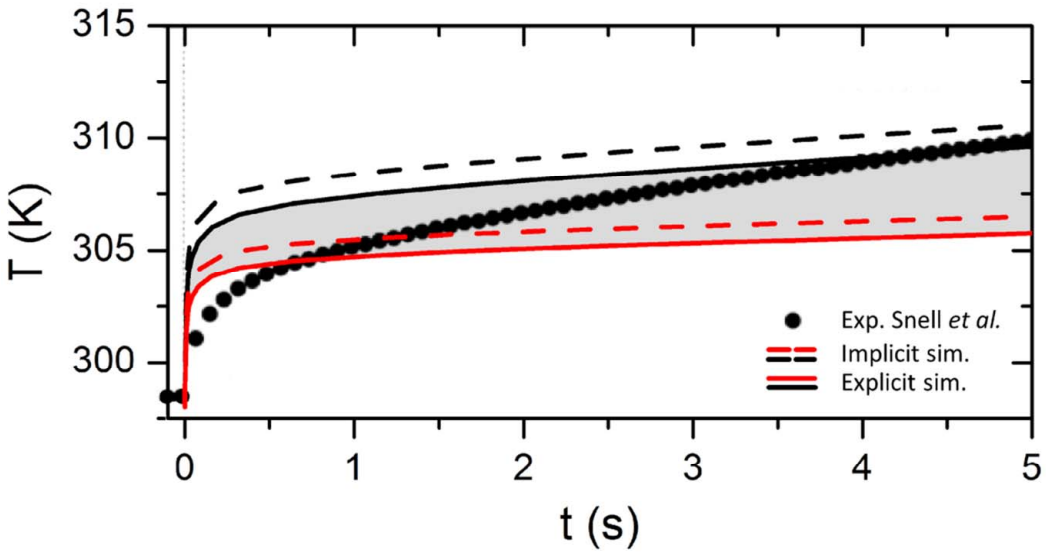


Figure 3 Comparison between the experimental (dots) and the simulation results (lines) for the validation case of the bead. The dashed and the solid lines represent the simulations with the implicit and the explicit definition of the heating source, respectively. The red lines correspond to the heating induced by the lowest photon flux density and the biggest bead radius compatible with the experimental error reported. The black lines correspond to the case with the highest photon flux density and the smallest bead radius compatible with the experimental error. The experimental data have been digitalized from Ref. (Snell *et al.*, 2007).

3.2. Prediction cases

3.2.1. Steady-state solution

REVIEW DOOL

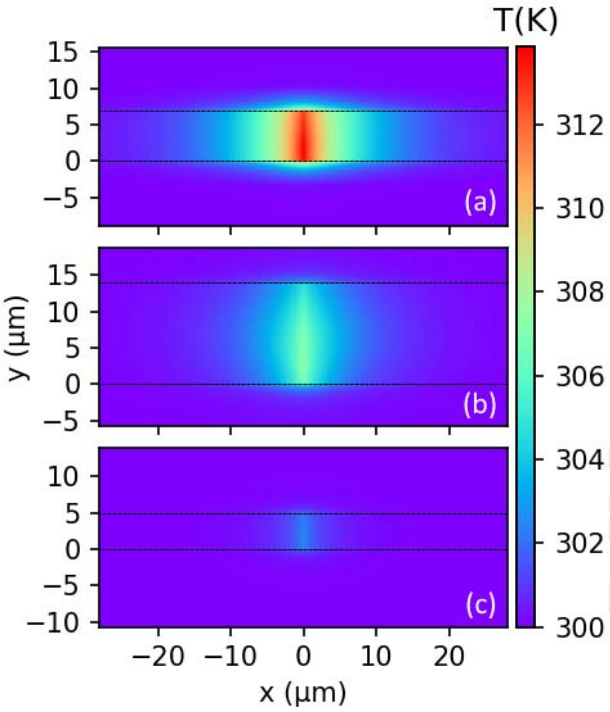


Figure 4 Calculated temperature spatial distribution induced in the crystals during irradiation in hypothetical steady-state conditions for samples (a) WBVB08, (b) WBAP13 and (c) WBAP14. The cross–section plane is located at half-thickness of the crystal. The nanobeam axis lies in the plane and is aligned along the y-direction, with the point (x=0 μm, y=0 μm) representing its incidence point on the crystal.

The steady-state solution of the model can be easily obtained by imposing a vanishing time derivative in Equation (2) and assuming that the heat source is time–independent, then $\Phi(t) = \bar{\Phi}_0$. The corresponding temperature distributions obtained defining the heat source with the explicit method are shown in Figure 4 for the samples WBVB08 (panel (a)), WBAP13 (panel (b)) and, WBAP14 (panel (c)). It can be observed that the temperature increase is significant only within about 30 μm from the beam, which confirms *a posteriori* the possibility of safely neglecting in the model the presence of the Ag contacts. Air heating can be appreciated only within a maximum distance of about 3 μm from the crystal surface, too. Therefore, the confinement of the temperature increase in these regions also confirms the validity of the boundary conditions assumed for the model. The maximum temperature T_{max} is about 314 K, 307 K and 303 K respectively for the samples WBVB08, WBAP13, and WBAP14.

This is in accordance with the fact that sample WBVB08 is the one with the highest maximum value $\bar{P}_{ex\,max}$. However, this seems not to be the only parameter that determines T_{max}. Indeed, although $\bar{P}_{ex\ max}$ has the lowest intensity in WBAP13, the temperature rise calculated in this case is not the

lowest one. This indicates that T_{max} is also strongly dependent on the energy spatial distribution of the heating source.

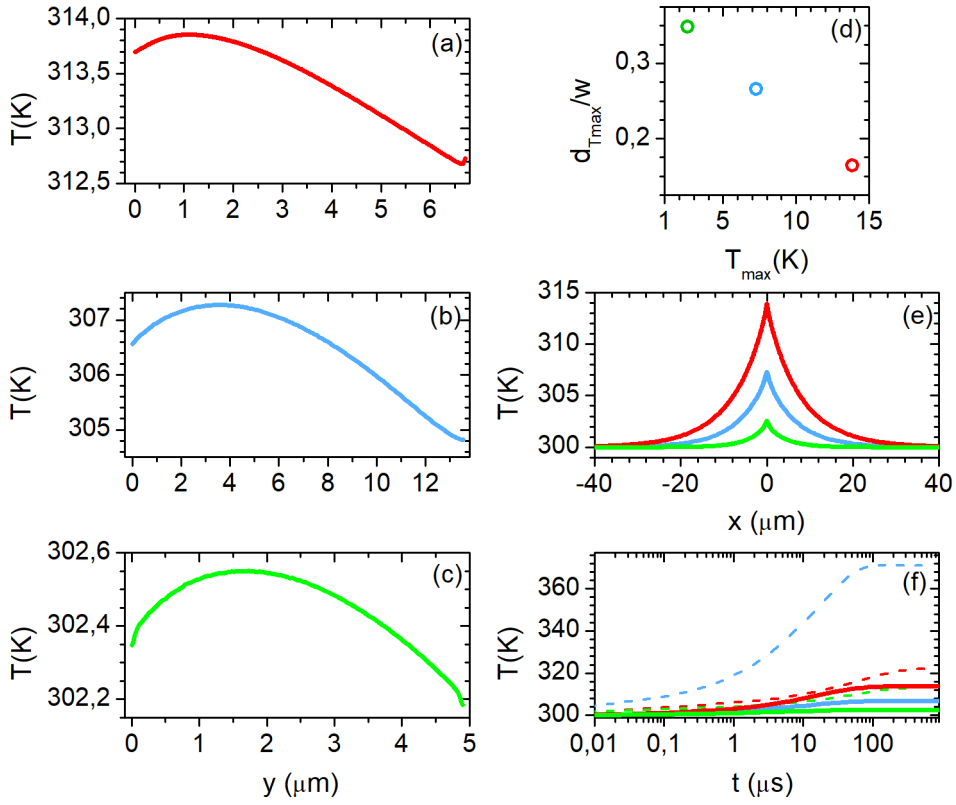


Figure 5 Spatial distribution of the temperature during irradiation in steady-state conditions according to the explicit method (MC+FEM simulations). Left panels show the temperature profile along the beam axis: (a) red line for WBVB08, (b) blue line for WBAP13 and (c) green line for WBAP14. With the same colours in right panels: (d) displays the linear correlation between the normalized distance of the T_{max} point as a function of the temperature increase, (e) reports the temperature distribution along the length of the crystals, plotted along a line parallel to the *x*-axis crossing the hottest point, and (f) shows the temperature temporal evolution at the T_{max} point as calculated by coupling Monte Carlo method with FEM (solid lines) and without Monte Carlo (dashed lines). At t=0 the irradiation starts, and the logarithmic scale has been used to highlight the different times at which temperatures saturate.

Figures 5(a), (b) and (c) display the corresponding temperature profiles calculated inside the crystals along the beam direction for samples WBVB08, WBAP13, and WBAP14, respectively. A temperature decrease can be noticed near the incident surface due to the cooling effect of air. In this regard, measuring the distance dT_{max} between the incidence surface and the position of T_{max}, and normalizing it with respect to the crystal width w, a linear correlation is found with T_{max} (Figure 5(d)). This implies that the higher the temperature, the closer (in relative units $d T_{max}/w$) the T_{max} point will

be to the X–ray incidence surface. The temperature behaviours in the crystal length direction (*x*–axis of the model) are reported in Figure 5 (e) for samples WBVB08, WBAP13, and WBAP14 in red, blue and green lines, respectively. The temperature profiles decay to room temperature less rapidly with the increase of T_{max}. Moreover, at most 40 μm away from the incidence point all the samples reach the ambient temperature, confirming the confinement of the heating effect.

3.2.2. Transient solution

The evolution of the temperature in the crystals under transient conditions, e.g. after turning the beam on at $t = 0$, can be studied by restoring the time derivative term in Equation (2), while keeping the heat source term Q equal to a time–independent constant $\bar{Q}$. The corresponding time behaviours shown in Figure 5(f) for samples WBVB08, WBAP13, and WBAP14 calculated at the hottest point are respectively represented with the solid red, blue and green curves. In the same figure, with the same colours, the corresponding behaviour calculated with the implicit method are represented with dashed lines. In general, three regimes can be distinguished: (i) an initial very fast increase of the temperature (typically less than few microseconds), (ii) a slowdown of the heating rate, and (iii) a final steady-state condition. Comparing the results from the implicit and the explicit models it is clear the overestimation of the heating response obtained with the former method.

3.2.3. Time-dependent solution

The implementation of the model with the pulsed nature of synchrotron radiation adds a remarkable complication to the problem by concentrating the absorbed power density in time intervals of tens of picoseconds and by modulating the pulse features in frequency and intensity. In order to obtain a closer description of the experimental situation, the real time dependence of the heat source term $Q = Q(t)$ was implemented in the model. The single time pulse of the beam is Gaussian in shape and has a root mean square duration RMS_t defined according to the relation $FWHM_t \cong 2.35\ RMS_t$. Therefore, in both the Equations (3) and (4), $\Phi(t)$ can be rewritten for each pulse as:

$$\Phi(t) = \Phi_0(t_{0,i})e^{-\left(\frac{2(t-t_{0,i})^2}{W_t^2}\right)}$$

where $W_t = \frac{FWHM_t}{\sqrt{2ln2}} \cong 0.85\ FWHM_t \cong 1.996\ RMS_t$ represents the pulse duration, $t_{0,i}$ the time of the i-th peak pulse, and $\Phi_0(t_{0,i})$ is the corresponding instantaneous photon flux. Since the time pattern of the beam flux is periodically repeated with a period T_{rev} = 2.82 μs, $\Phi_0(t_{0,i})$ can be determined for each mode of the storage ring by requesting that:

$$\int_t^{t+T_{rev}} \Phi_0(t')dt' = \bar{\Phi}_0 T_{rev} \quad (2)$$

The values of the parameters used to describe the time modulation of the synchrotron radiation are listed in Table 4.

REVIEW DOCUMENT

Table 4 Parameters used to determine the peak power density at the beam incidence point for the case of pulsed heat source. For the 7/8+1 mode, three values are indicated for $\Phi_0(t_{0,i})$ corresponding to the three different types of peaks contained in the 7/8+1 filling pattern.

Sample	Mode	RMS_t (ps)	$FWHM_t$ (ps)	W_t (ps)	$\Phi_0(t_{0,i})$ (10^{13} ph s^{-1})
WBVB08	16 bunch	48	112.8	95.88	43.84
WBAP13					27.77
WBAP14	7/8+1	20	47	39.95	0.63
					2.76
					5.51

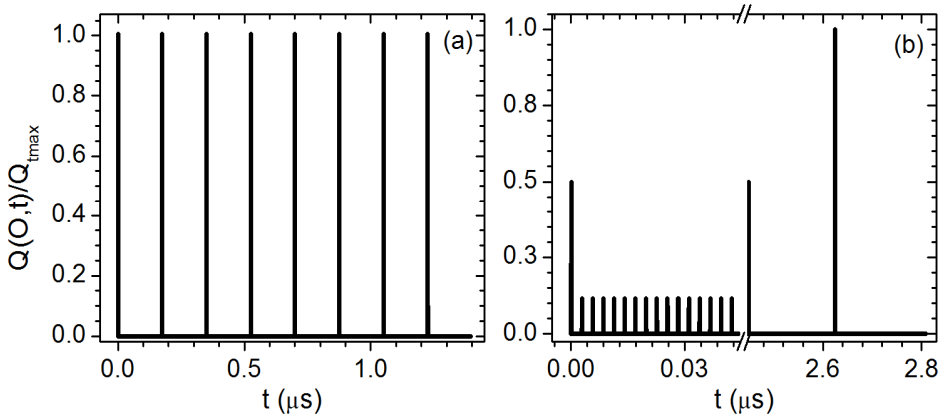


Figure 6 Temporal evolution of the normalized power density $Q(O,t)/Q_{tmax}$ for the two filling modes of the storage ring: panel (a) 16 bunch mode, corresponding to irradiation of samples WBVB08 and WBAP13 (only the first 8 bunches after t=0 are shown), and panel (b) 7/8+1 mode, corresponding to irradiation of sample WBAP14 (different portions of the period are shown).

In 16-bunch filling mode, used for samples WBVB08 and WBAP13, all of the pulses are equal and $\Phi_0(t_{0,i}) = \frac{\overline{\Phi_0} T_{rev}}{16 W_t \sqrt{\frac{\pi}{2}}}$. Figure 6(a) shows the time behaviour of the power density at the beam incidence point $Q(O,t)$ corresponding to the first eight bunches, normalized to their peak value Q_{tmax} which corresponds to the most intense power density at the incidence point obtained at $t_{0,i}$, i.e. when the absolute maximum flux $\Phi_0(t_{0,i})$ is reached. On the other hand, in the 7/8+1 mode (sample WBAP14) three different kinds of pulses are present, having intensities of 0.23, 1 and 2 mA/bunch. The instantaneous flux corresponding to the smallest peak can be obtained from Eq.(2) as $\Phi_0(t_{0,i}) =$

$\frac{0.23\,\overline{\Phi_0}T_{rev}}{203.64\,W_t\sqrt{\frac{\pi}{2}}}$. The time evolution of the normalized power density $Q(O,t)/Q_{tmax}$ for sample WBAP14 is represented in Figure 6(b) for two representative portions of the time pattern.

16 bunch irradiation of WBVB08 and WBAP13

The comparison between the temperature time behaviours of the transient and the time-dependent solutions, as calculated at the hottest point with the explicit method, is reported in Figure 7(a) for WBVB08 and in panel (b) for WBAP13. Because of the dense time packing of the X–ray energy, the temperature rapidly increases in correspondence with the pulse arrival. Indeed, the instantaneous heating power density are four orders of magnitude larger than the respective steady-state cases. In the first pulse, the temperature rises to a maximum of about 340 K and 312 K within about 350 ps, respectively, in samples WBVB08 and WBAP13. Then, it slowly decreases in the interval between two pulses, reaching a minimum temperature of about 300 K immediately before the second pulse arrives. In Figure 7(a) and 7(b), it is also possible to appreciate how the difference between the transient (red and blue curves) and the pulsed solutions (corresponding black curves) becomes more evident with increasing the maximum temperature achieved with the pulsed heat source. This fact clarifies how considering synchrotron experiments measurements and simulations, that average the sample temperature over time scales of the order of 100 ns or more, can result in an underestimation of the real instantaneous sample temperature.

In Figure 7(d) and 7(e), a blow-up of the first temperature peak, as calculated with the explicit (solid line) and implicit (dashed lines) methods, is reported for sample WBVB08 and WBAP13 respectively. It is possible to observe that the temperature increases simulated with the implicit method are about one order of magnitude higher than the ones obtained with the explicit method. Precisely, an overestimation of about 500 K and of 90 K for the samples WBVB08 and WBVB13 is obtained with the implicit method, respectively. By comparing these results with the ones shown in Figure 5(f), for the corresponding transient cases, it can be observed how the temperature difference between the implicit and explicit methods becomes bigger when the time modulation of the heat source is considered.

REVIEW DOCUMENT

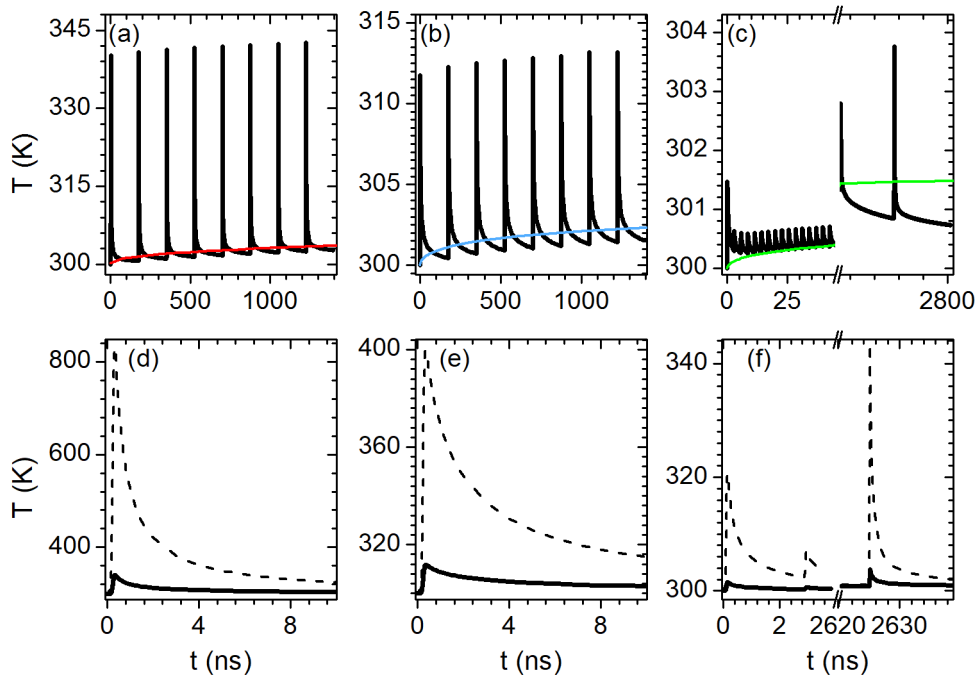


Figure 7 Simulation of the X-ray-induced heating calculated at the point of maximum temperature by considering the time pattern of the source. The predictions obtained with the explicit method for samples WBVB08, WBAP13, and WBAP14 are shown in panel (a), (b) and (c), respectively. Black lines represent the time-dependent studies and coloured lines show the corresponding transient behaviour in steady-state conditions, already shown in Figure 5(e). Following the same sample order, in panel (d), (e) and (f) the corresponding simulations are compared with the ones calculated with the implicit method (dashed lines).

7/8+1 irradiation of WBAP14

The heating evolution calculated with the explicit method at the maximum temperature point of WBAP14 is reported in Figure 7(c). The more complex structure of the irradiation time pattern is reflected in the temperature evolution of the sample: the two temperature peaks of about 301.5 K and 303 K (at t≈0 and t≈2500 ns), corresponding to the two 1 mA bunches of the storage ring, delimit the train of 868 smaller bunches generating lower temperature peaks, whose maxima lie between 300 K and 301 K. The highest temperature peak at about 304 K corresponds to the single bunch of 2 mA (at t≈2600 ns). It can be noted that the temperature increase is lower than the cases in 16-bunch mode. This is consistent with the peak value of the heat source of 1.9×10^{17} W/ m^3 (2mA pulse), which is considerably less than the ones calculated for samples WBVB08 and WBAP13 of 1.3×10^{18} W/m^3 and 3.2×10^{17} W/m^3, respectively. By comparing the time–dependent to the transient solution (green line), it can be noticed that in the region of the closely spaced pulses at t ≈ 0 ns the first three peaks have a minimum temperature which is higher than the transient behaviour. This is due to the presence of the 1 mA peak at t ≈ 0 in the power density *Q(t)*. Indeed, after the repetition of the 868 pulses, the

temperature of the transient case is stabilized and the baseline of the pulsed profile falls below the transient behaviour as expected, because the transient solution should represent a sort of time average of the real pulsed regime. A maximum difference of about 2 K from the transient behaviour can be detected in this region around t ≈ 2440–2800 ns for the last two pulses.

In Figure 7(f), the temperature evolution calculated from the explicit method is compared with the one derived from the implicit method for the most intense peaks observed in sample WBAP14. A maximum overestimation of the heating of about 40 K is obtained. Therefore, the lower heating predicted with the explicit method can be considered as an improvement in the accuracy of the model. This fact, not only clarifies the role of the absorbed energy spatial distribution in the thermal phenomenon, but it also allows us to effectively determine the impact of the thermal effects in the observed material property changes. From this point of view, the hypothesis that very high temperature peaks could have been induced by X–rays during these experiments must be rejected. Anyway, the possibility that synchrotron pulses may induce thermal stresses in the crystals cannot be excluded. Indeed, plastic deformation and cracks formation can occur due to the strong thermal gradient (Moshe *et al.*, 2000, Nicholson *et al.*, 2001, Hau-Riege, 2012). Moreover, even in the case that thermal and mechanical phenomena are not important, the repetitive pulsed irradiation can cause thermal fatigue and fracture (De Castro *et al.*, 2010, Ryutov, 2003). The numerical assessment of these possibilities requires more dedicated investigations.

The temperature distributions calculated at the instant of maximum temperature increase with the explicit method are reported in Figure 8. For all of the samples the heating effects are almost completely confined within the beam spot–size.

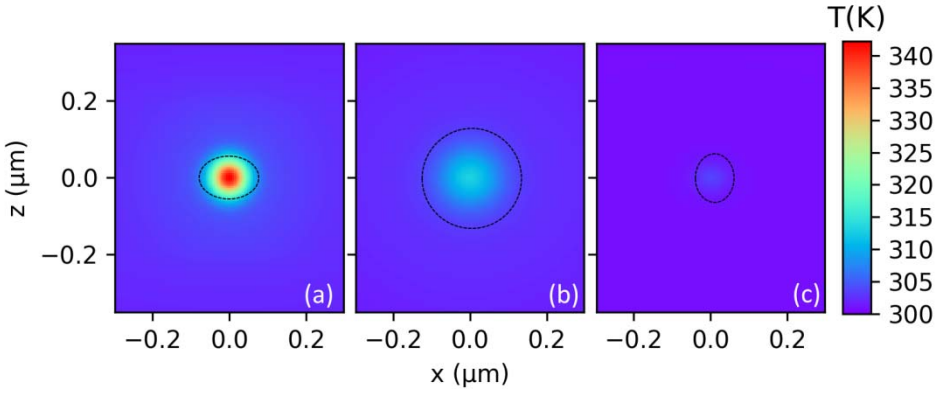


Figure 8 Calculated temperature spatial distribution induced by the nanobeams in the pulsed regime as calculated with the explicit method for samples WBVB08 (a), WBAP13(b), and WBAP14 (c). The *xz* cross-section planes pass across the hottest points and correspond to the instant of maximum temperature reached by each sample. Black contour lines indicate the half–maximum intensity points of the incident beam.

3.2.4. Adiabatic approximation

It is important to note that without considering the photo–atomic and the electron interactions, it is not possible to correctly estimate the instantaneous temperature increase for the experiments. On the contrary, if the spatial extension of these interaction is given by any simulation code, it is possible to exploit the adiabatic approximation to obtain a preliminary estimation of the results of the numerical solution of the heat transfer equation. Indeed, if we consider the predictive cases corresponding to the $Bi_2Sr_2CaCu_2O_{8+\delta}$ X–ray nanopatterning experiments, the thermal diffusivity of the material is given by $\alpha = \frac{k_{ab}}{\rho C_p} = 2.09 \times 10^{-6}$ m^2 s^{-1}. This implies that for any typical radius Δr of the cylindrical volume where energy deposition takes place around the beam axis, the time Δt needed by the heat to diffuse out of this region is of the order of $\Delta r^2/\alpha$. It can be easily checked that, even in the case of a very small Δr value in the order of magnitude of 100 nm, then $\Delta t \approx 4.8$ ns, which is much longer that any X–ray pulse duration reproduced by our numerical simulations (20-50 ps). This means that the energy deposition is so fast that during each pulse there is no time for the heat to diffuse out of the energy deposition region, which makes the adiabatic approach meaningful. Therefore, during such a short timescale, the energy deposition volume can be considered as isolated from the rest of the sample, and the corresponding temperature increase can be calculated, which is expected to correspond to the maximum temperature reached in the sample.

Therefore, the definition of the energy deposition volume is an important step. Due to the irradiation geometry, this volume can be identified with a cylindrical volume with radius Δr and height Δl. Keeping in mind that we are interested in estimating the maximum temperature to be observed in the sample, it is expected that the point where this temperature is reached has to be close to the sample surface, which means that this point lies in the sample within a depth that is much less than the X-ray attenuation depth λ. Therefore, the choice $\Delta l = \lambda/10$ is expected both to contain the maximum temperature point and to be reasonably uniform in energy deposition and in temperature increase. Concerning the radius Δr, this can be estimated only on the basis of the MC results. By fitting to Gaussian curves the cross-section profiles at the sample surface of the energy deposition curves plotted in Figure 2, the $FWHM_{xz}$ values reported in Table 5 can be obtained.

Table 5 Parameters used to estimate the instantaneous maximum temperature ΔT at the peak photon flux in adiabatic approximation. λ represents the X-ray attenuation depth, $FWHM_{xz}$ refers to the transverse Gaussian profile of the energy deposition, and E_{bunch} is the energy of all of the photons of a single bunch

Sample	λ (μm)	$FWHM_{xz}$ (nm)	E_{bunch} (pJ)	ΔT (K)

REVIEW DOCUMENT

WBVB08	17.8	310	147	34.6
WBAP13	16.9	520	91.4	8.03
WBAP14 (smallest peaks)	18.3	470	3.9	0.39

Therefore, a natural choice in this respect consists in assuming $\Delta r = FWHM_{xz}/2$. Then, the maximum temperature increase ΔT can be estimated by considering all of the energy absorbed by the cylinder during a single bunch as heat adiabatically delivered to it:

$$\Delta T = \frac{E_{bunch}(1-e^{-0,1})}{mC_p},$$

Where E_{bunch} is the energy corresponding to all of the photons of a single bunch, and $m = \rho\pi\Delta r^2\Delta l$. The corresponding values are listed in Table 5 and compare reasonably well with the results from the numerical solutions.

Conclusions

In this work, the Fourier heat equation was solved with the finite element method to simulate the X–ray heating effects induced by third-generation synchrotrons in inorganic materials. Two approaches were used to defined the heat source term. In addition to the already reported approach, in which the heat source is implicitly approximated by using the experimental parameters coming from the beam profile and the material attenuation length, we proposed a second method in which the heat source is defined explicitly. This is done using a Monte Carlo method which explicitly consider the photons and particles interactions involved in the absorption and relaxation processes of the target. Both the models were applied to simulate the heating measurements carried out by Snell et al. in a millimetric glass bead (Snell *et al.*, 2007) finding a good agreement. However, it also emerges how a control of the experimental parameter is fundamental to accurately model the system and reduce the variation of the predicted behaviour.

In the other scenario explored, the role of heating in three example of X–ray nanopatterning experiments, performed in $Bi_2Sr_2CaCu_2O_{8+\delta}$ microcrystals (Mino *et al.*, 2017, Pagliero *et al.*, 2014, Truccato *et al.*, 2016), is predicted. For these cases, the theoretical prediction of the heating behaviours was studied modelling the heat source in stationary and time–dependent conditions —i.e. the filling pattern of the storage ring is considered when modulating in time the heat source.

In the stationary case, the maximum temperature achieved is found to be dependent not only on the power density, but also on the spatial distribution of the heat source in the plane normal to the beam.

REVIEW DOCUMENT

Moreover, an overestimation of up tens of degrees is obtained with the implicit method. This strong difference was attributed to the energy redistribution that takes place due to photolectron emission and transport. This implies that the more accurate definition of the power density distribution in the explicit method is fundamental. In the time–dependent problem, in which the pulsed behaviour of synchrotrons is considered, the heating phenomenon was demonstrated to be roughly proportional to the instantaneous peak value of the absorbed power density. Finally, in this more complex regime, the comparison between the implicit and explicit methods highlighted the crucial impact of the power density distributions. Indeed, in the implicit method, which disregards the energy distribution taking place with photo–absorption events, an overestimation of the thermal effects of the order of hundreds of degrees is predicted. Conversely, if the spatial redistribution of the absorbed energy is explicitly considered, an adiabatic approach can estimate the temperature increase reasonably well.

Ultimately, from the point of view of the X–ray nanopatterning process, the calculated instantaneous temperature increase, for the three considered samples, varies from a few degrees to tens of degrees. Therefore, by considering that $Bi_2Sr_2CaCu_2O_{8+\delta}$ has a melting temperature of about 860 °C, an ordinary melting process can be excluded.

Acknowledgements The authors thank the ESRF for the beamtime allocated. M.T. and V.B. acknowledge partial support from the “Department of Excellence” (L.232/2016) grant, funded by the Italian Ministry of Education, University and Research (MIUR). This work has been partly carried out under project NANO-X jointly approved and funded by University of Torino and Compagnia di San Paolo.

REVIEW DOCUMENT

Supporting information

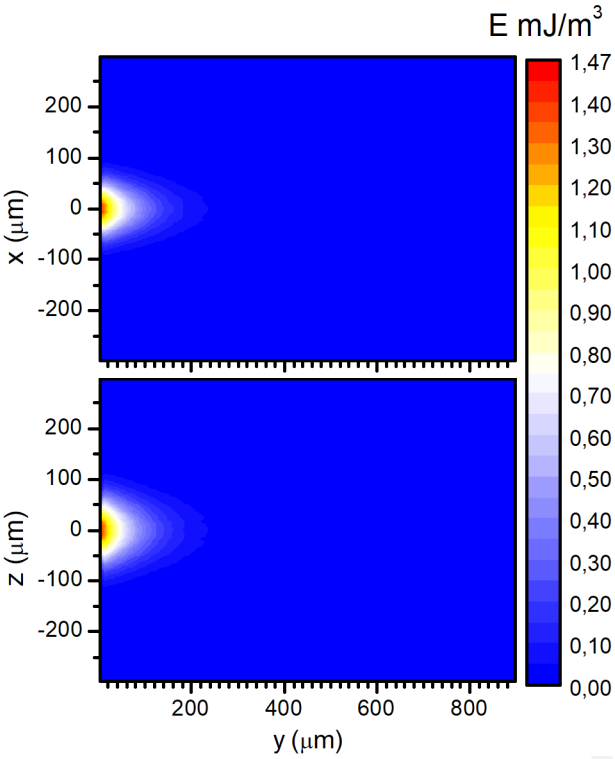


Figure S1 2D plots of the energy spatial distributions evaluated by the MCNP6 code for the glass bead. The *yx*– and *yz*–planes of symmetry are shown.

REVIEW DOCUMENT

References

https://mcnp.lanl.gov/.
Adriaens, A., Quinn, P., Nikitenko, S. & Dowsett, M. G. (2013). *Anal. Chem.* **85**, 9556-9563.
Archer, D. G. (1993). *J. Phys. Chem. Ref. Data* **22**, 1441-1453.
Bahk, S. W., Rousseau, P., Planchon, T. A., Chvykov, V., Kalintchenko, G., Maksimchuk, A., Mourou, G. A. & Yanovsky, V. (2004). *Opt. Lett.* **29**, 2837-2839.
Bonino, V., Agostino, A., Prestipino, C., Hernandez, O., Fretto, M., Mino, L. & Truccato, M. (2018). *Crystengcomm* **20**, 6667-6676.
Bonino, V., Mino, L., Agostino, A., Prestipino, C., Fretto, M. & Truccato, M. (2019). SPIE Optics + Optoelectronics, **11035**, 110350I.
Bras, W. & Stanley, H. (2016). *J. Non-Cryst. Solids* **451**, 153-160.
Burghartz, S. & Schulz, B. (1994). *J. Nucl. Mater.* **212**, 1065-1068.
COMSOL Multiphysics®. Version 4.3b.
Crommie, M. F. & Zettl, A. (1990). *Physical Review B* **41**, 10978-10982.
De Castro, A. R. B., Vasconcellos, A. R. & Luzzi, R. (2010). *Rev. Sci. Instrum.* **81**.
Feldman, Y., Lyahovitskaya, V., Leitus, G., Lubomirsky, I., Wachtel, E., Bushuev, V. A., Vaughan, G., Barkay, Z. & Rosenberg, Y. (2009). *Applied Physics Letters* **95**.
Gadermaier, C., Alexandrov, A. S., Kabanov, V. V., Kusar, P., Mertelj, T., Yao, X., Manzoni, C., Brida, D., Cerullo, G. & Mihailovic, D. (2010). *Phys. Rev. Lett.* **105**.
Gnodtke, C., Saalmann, U. & Rost, J. M. (2009). *Phys. Rev. A* **79**.
Hau-Riege, S. P. (2012). *High-Intensity X-rays - Interaction with Matter: Processes in Plasmas, Clusters, Molecules and Solids*. Wiley.
Henke, B. L. G., E.M.; Davis J.C. (1993). *Atomic Data and Nuclear Data Tables* **54**, 181-342.
Hsu, P.-C., Chen, Y.-S., Hwu, Y., Je, J. H., Margaritondo, G. & Tok, E. S. (2015). *J. Synchrot. Radiat.* **22**, 1524-1527.
Lide, D. R. (2003). *Handbook of chemistry and physics*. CRC, Boca Raton.
Lindgren, M., Currie, M., Williams, C., Hsiang, T. Y., Fauchet, P. M., Sobolewski, R., Moffat, S. H., Hughes, R. A., Preston, J. S. & Hegmann, F. A. (1999). *Applied Physics Letters* **74**, 853-855.
Liu, X., Du, D. & Mourou, G. (1997). *IEEE J. Quantum Electron.* **33**, 1706-1716.
London, R. A., Bionta, R. M., Tatchyn, R. O. & Roesler, S. (2001). *Proceedings of SPIE-The International Society for Optical Engineering*, Vol. 4500. *Optics for Fourth-Generation X-Ray Sources,* edited by R. O. Tatchyn, A. K. Freund & T. Matsushita, pp. 51-62. Bellingham: Spie-Int Soc Optical Engineering.
Martinez-Criado, G., Villanova, J., Tucoulou, R., Salomon, D., Suuronen, J. P., Laboure, S., Guilloud, C., Valls, V., Barrett, R., Gagliardini, E., Dabin, Y., Baker, R., Bohic, S., Cohen, C. & Morse, J. (2016). *J. Synchrot. Radiat.* **23**, 344-352.
Martis, V., Nikitenko, S., Sen, S., Sankar, G., van Beek, W., Filinchuk, Y., Snigireva, I. & Bras, W. (2011). *Cryst. Growth Des.* **11**, 2858-2865.
Mino, L., Bonino, V., Agostino, A., Prestipino, C., Borfecchia, E., Lamberti, C., Operti, L., Fretto, M., De Leo, N. & Truccato, M. (2017). *Sci Rep* **7**, 9066
Mino, L., Bonino, V., Picollo, F., Fretto, M., Agostino, A. & Truccato, M. (2019). *Adv. Electron. Mater.* **5**.
Mino, L., Borfecchia, E., Segura-Ruiz, J., Giannini, C., Martinez-Criado, G. & Lamberti, C. (2018). *Reviews of Modern Physics* **90**, 65.
Mirzoev, F. K., Panchenko, V. Y. & Shelepin, L. A. (1996). *Uspekhi Fiz. Nauk* **166**, 3-32.
Moshe, E., Eliezer, S., Henis, Z., Werdiger, M., Dekel, E., Horovitz, Y., Maman, S., Goldberg, I. B. & Eliezer, D. (2000). *Applied Physics Letters* **76**, 1555-1557.
Natividad, E., Castro, M., Burriel, R. & Angurel, L. A. (2006). *J. Therm. Anal. Calorim.* **84**, 307-316.
Neutze, R., Wouts, R., van der Spoel, D., Weckert, E. & Hajdu, J. (2000). *Nature* **406**, 752-757.
Nicholson, J., Nave, C., Fayz, K., Fell, B. & Garman, E. (2001). *Nucl. Instrum. Methods Phys. Res. Sect. A-Accel. Spectrom. Dect. Assoc. Equip.* **467**, 1380-1383.
Pagliero, A., Mino, L., Borfecchia, E., Truccato, M., Agostino, A., Pascale, L., Enrico, E., De Leo, N., Lamberti, C. & Martinez-Criado, G. (2014). *Nano Lett.* **14**, 1583-1589.
Rosenthal, M., Doblas, D., Hernandez, J. J., Odarchenko, Y. I., Burghammer, M., Di Cola, E., Spitzer, D., Antipov, A. E., Aldoshin, L. S. & Ivanov, D. A. (2014). *J. Synchrot. Radiat.* **21**, 223-228.
Ryutov, D. D. (2003). *Rev. Sci. Instrum.* **74**, 3722-3725.
Seitz, F. & Turnbull, D. (1956). Vol. 2. *Solid State Physics*, pp. 307-449: Academic Press.
Snell, E. H., Bellamy, H. D., Rosenbaum, G. & van der Woerd, M. J. (2007). *J. Synchrot. Radiat.* **14**, 109-115.
Stanley, H. B., Banerjee, D., van Breemen, L., Ciston, J., Liebscher, C. H., Martis, V., Merino, D. H., Longo, A., Pattison, P., Peters, G. W. M., Portale, G., Sen, S. & Bras, W. (2014). *Crystengcomm* **16**, 9331-9339.
Subramanian, M. A., Torardi, C. C., Calabrese, J. C., Gopalakrishnan, J., Morrissey, K. J., Askew, T. R., Flippen, R. B., Chowdhry, U. & Sleight, A. W. (1988). *Science* **239**, 1015-1017.
T. Goorley, M. James, T. Booth, F. Brown, J. Bull, J. Cox & Durkee, J. *"Initial MCNP6 Release Overview", Nuclear Technology, 180, pp 298-315 (Dec 2012).*
Torsello, D., Mino, L., Bonino, V., Agostino, A., Operti, L., Borfecchia, E., Vittone, E., Lamberti, C. & Truccato, M. (2018). *Phys. Rev. Mater.* **2**.
Truccato, M., Agostino, A., Borfecchia, E., Mino, L., Carat, E., Pagliero, A., Adhlakha, N., Pascale, L., Operti, L., Enrico, E., De Leo, N., Fretto, M., Martinez-Criado, G. & Lamberti, C. (2016). *Nano Lett.* **16**, 1669-1674.
Truccato, M., Agostino, A., Rinaudo, G., Cagliero, S. & Panetta, M. (2006). *Journal of Physics-Condensed Matter* **18**, 8295-8312.
Tu, F., Spath, A., Drost, M., Vollnhals, F., Calderon, S. K., Fink, R. H. & Marbach, H. (2017). *J. Vac. Sci. Technol. B* **35**.
US Standard Atmosphere (1976).
Wallander, H. & Wallentin, J. (2017). *J. Synchrot. Radiat.* **24**, 925-933.

REVIEW DOCUMENT

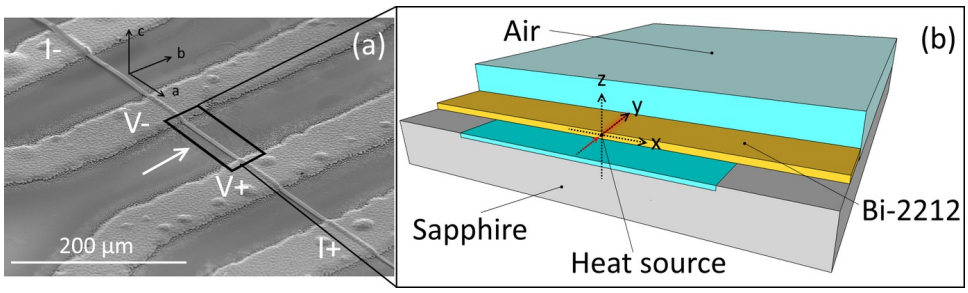


Figure 1

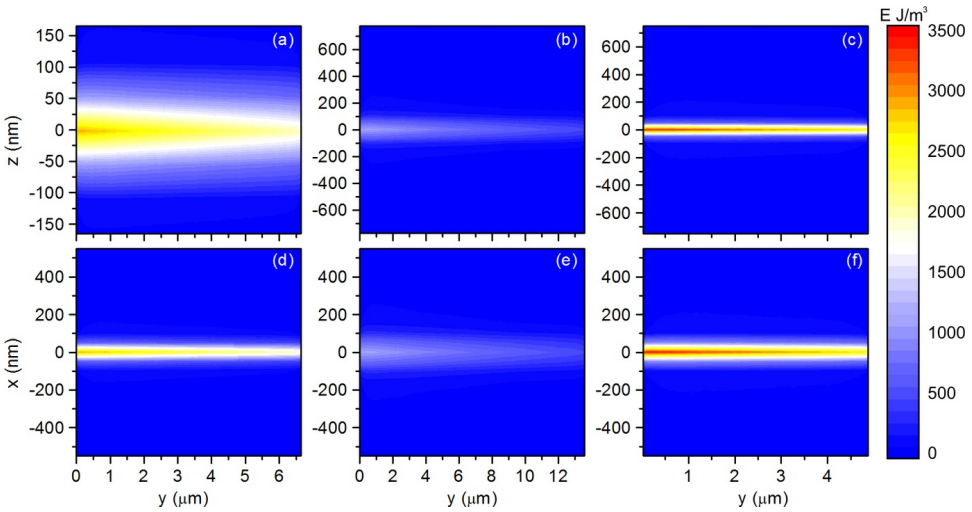

E J/m3
3500
3000
2500
2000
1500
1000
500
0
(a)
(b)
(c)
(d)
(e)
(f)
z (nm)
x (nm)
y (μm)
y (μm)
y (μm)

Figure 2

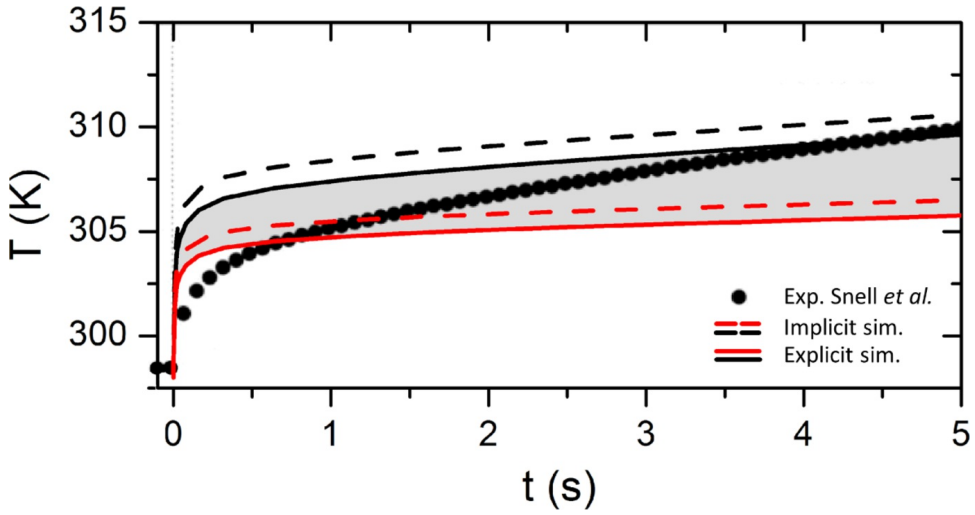

315
310
305
300
T (K)
0
1
2
3
4
5
t (s)
Exp. Snell et al.
Implicit sim.
Explicit sim.

Figure 3

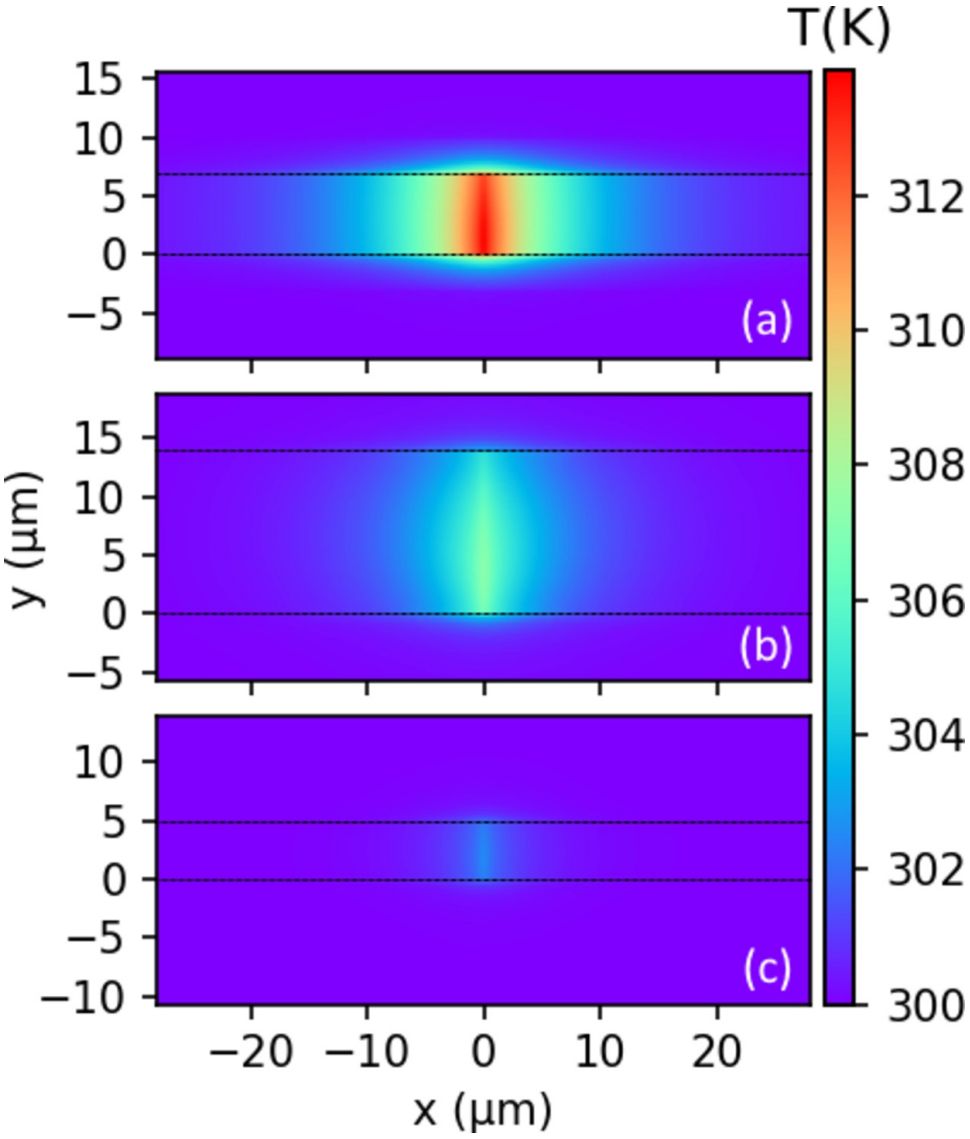

T(K)
312
310
308
306
304
302
300
(a)
(b)
(c)
y (μm)
x (μm)
15
10
5
0
−5
−10
−20
−10
0
10
20

Figure 4

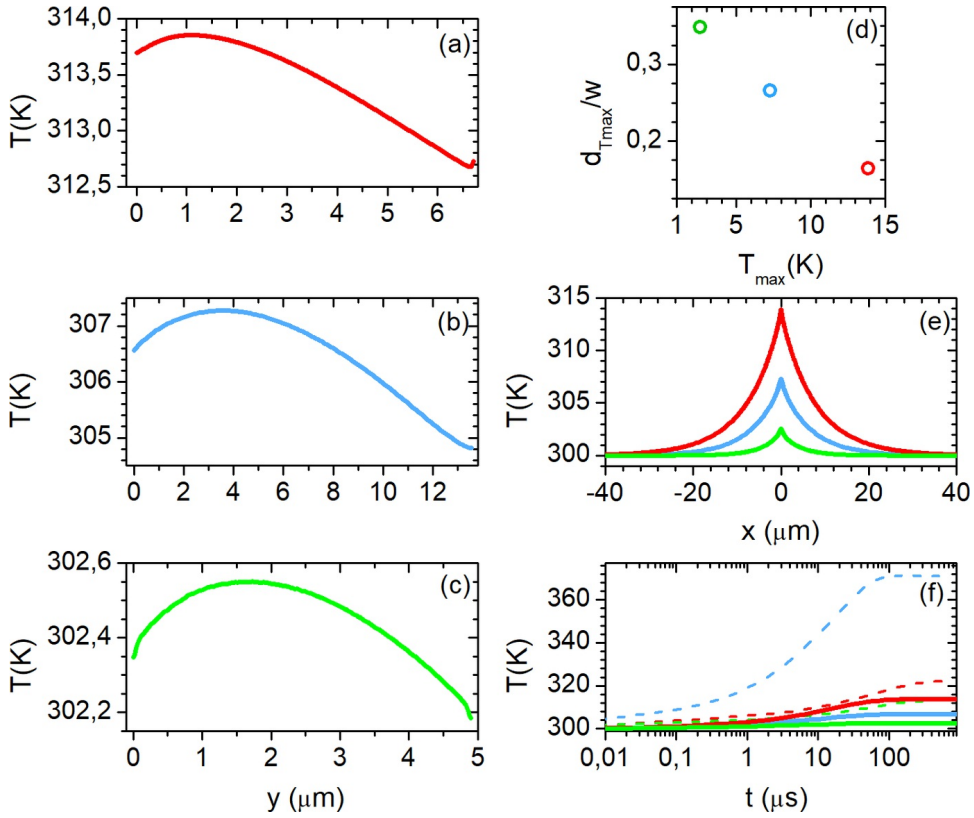

(a)
T(K)
314,0
313,5
313,0
312,5
0 1 2 3 4 5 6
(b)
T(K)
307
306
305
0 2 4 6 8 10 12
(c)
T(K)
302,6
302,4
302,2
0 1 2 3 4 5
y (μm)
(d)
d_{Tmax}/w
0,3
0,2
1 5 10 15
T_{max}(K)
(e)
T(K)
315
310
305
300
-40 -20 0 20 40
x (μm)
(f)
T(K)
360
340
320
300
0,01 0,1 1 10 100
t (μs)

Figure 5

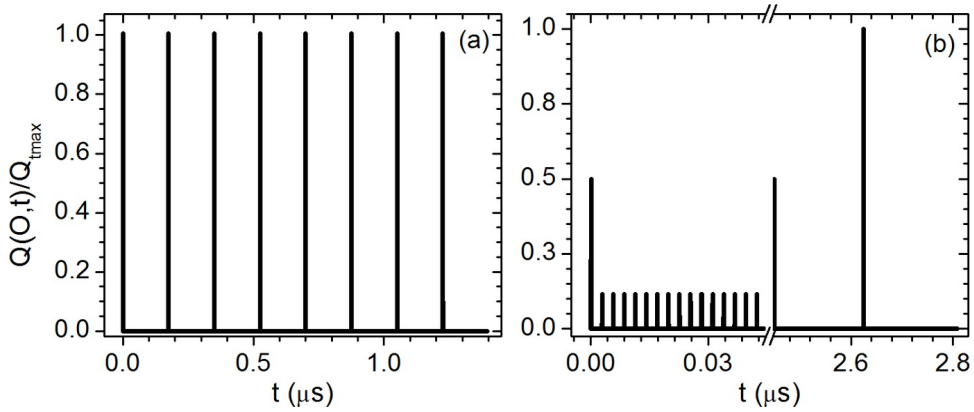


Figure 6

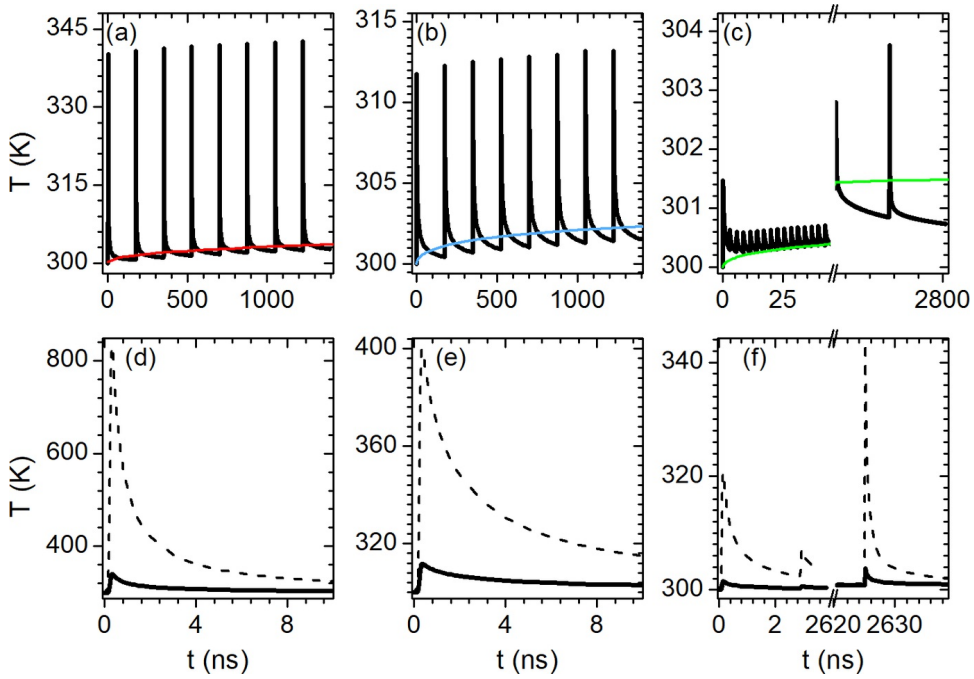


Figure 7

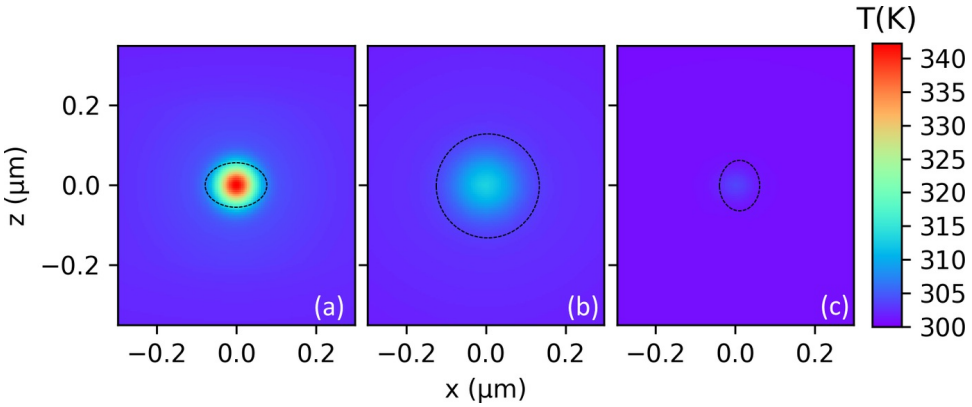

T(K)
340
335
330
325
320
315
310
305
300
z (μm)
0.2
0.0
−0.2
(a)
(b)
(c)
−0.2
0.0
0.2
x (μm)

Figure 8